J. Fluid Mech. (2021), *vol*. 924, A28, doi:10.1017/jfm.2021.619

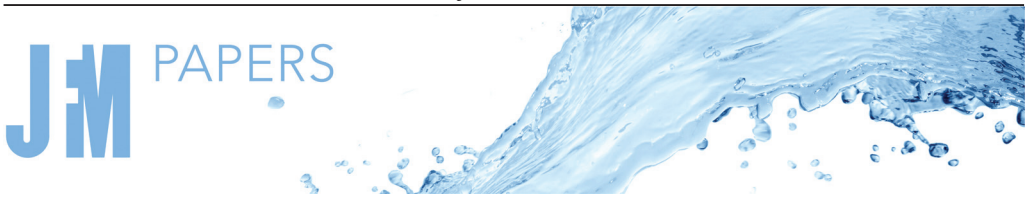

The persistence of large-scale circulation in Rayleigh–Bénard convection

Ping Wei†

School of Aerospace Engineering and Applied Mechanics, Tongji University, Shanghai 200092, PR China

(Received 25 December 2020; revised 14 June 2021; accepted 2 July 2021)

The time-averaged strength $\langle\delta\rangle/\Delta$ of a convective cellular pattern and large-scale circulation (LSC) in the turbulence regime of turbulent Rayleigh–Bénard convection exhibits a sequence of sharp changes with the Rayleigh number Ra. Changes occur when Ra reaches transition values between the conduction, convection, chaotic, transition, soft turbulence and hard turbulence regimes. Measurements were taken from two cylindrical cells with Plexiglas walls and nitrogen gas as the working fluid. The data cover the range $10^3 \lesssim Ra \lesssim 10^9$ at $Pr = 0.72$, where Pr is the Prandtl number and $\Gamma \equiv D/H = 1.00$ is the aspect ratio (diameter over height). The cellular pattern strength δ grows continuously as Ra exceeds the critical value $Ra_c = 7300$ for the wall admittance $C = 2.02$ in the convection regime. In the oscillation regime, the temperature power spectra at the sidewall show an oscillatory frequency peak. In the chaotic regime, δ is diminished as Ra increases. In the transition regime, $\langle\delta\rangle/\Delta$ continues to decrease, nearly to 0. Under soft turbulence where the LSC is formed, $\langle\delta\rangle$ grows with Ra as a cellular pattern in the convection regime, suggesting that LSC reflects a cellular pattern. Under hard turbulence, the LSC flow strength decreases as Ra increases. The Reynolds number Re was also measured based on the LSC turnover time, and it was found that two power laws, $\langle\delta\rangle/\Delta \times Ra/Pr = 0.007Re^{3.0}$ and $\langle\delta\rangle/\Delta \times Ra/Pr = 15.4Re^{1.76}$, fit the data for $Re < 400$ and $Re > 400$, respectively.

Key words: Bénard convection, buoyancy-driven instability, turbulent convection

1. Introduction

Rayleigh–Bénard convection (RBC), which refers to a layer of fluid confined between parallel horizontal plates and heated from below, is the ideal system for studying convection occurring in both natural and engineering processes (see, e.g. Brent, Voller & Reid 1988; Hunt & Linden 1999; Marshall & Schott 1999; Rahmstorf 2000; Hartmann, Moy & Fu 2001). RBC is determined by the Rayleigh number $Ra = \alpha g \Delta L^3/\kappa\nu$ and the

† Email address for correspondence: ping.wei@tongji.edu.cn

Prandtl number $Pr = \nu/\kappa$, where α is the isobaric thermal expansion coefficient, g is the gravitational constant of acceleration, Δ is the temperature difference between the plates, L is the spacing between the plates, κ is the thermal diffusivity coefficient and ν is the kinematic viscosity. In addition, because physically realisable studies use cells with a finite lateral extent, the aspect ratio $\Gamma \equiv D/L$ of the sample is another relevant parameter, where D is the lateral size of the sample, for instance, the diameter of a cylindrical cell.

The global response of a system to a thermal driving force is reflected in the vertical transport of heat from the bottom plate to the top plate, and such transport is expressed in dimensionless form by the Nusselt number $Nu = \lambda_{eff}/\lambda$, where the effective conductivity λ_{eff} is given by $\lambda_{eff} = QL/(\pi(D/2)^2\Delta)$, with Q being the heat flux and λ being the thermal conductivity of the quiescent fluid. Another parameter that reflects the system response is the extent of turbulence, expressed in terms of a characteristic velocity amplitude U. Turbulent RBC can also be described by the dimensionless Reynolds number $Re = UL/\nu$.

The Nusselt number is equal to 1 when the driving force determined as Ra is small enough and heat is only transferred by the pure conduction of fluid. When $Ra > Ra_c$, where Ra_c is the critical value that represents the onset of convection, convective flows form a pattern and contribute to heat transport. In theory the value of Ra_c was calculated by Jeffreys (1928) and found to be 1708 for a sample of infinite lateral extent and with rigid isothermal boundary conditions at the top and bottom plates. This bifurcation was also predicted to be supercritical (Jeffreys 1928; Schlüter, Lortz & Busse 1965). The Nu increases continuously and linearly as Ra exceeds Ra_c. This was confirmed with high resolution by numerous experiments. The pattern formation is an interesting aspect of RBC, which has been studied extensively in the sample of large $\Gamma(>5)$ and at low $Ra(<10^5)$.

As Ra further increases, the flow inside RBC is so strong that it is considered as turbulent convection (Ahlers 2009; Ahlers, Grossmann & Lohse 2009; Lohse & Xia 2010), which is mainly studied in small $\Gamma(O(1)$ or less) samples and characterised by high Ra (up to 10^{17}). The turbulent fluid flow in RBC for $Ra > 10^6$ experiences considerable fluctuation but tends to become organised into a single convection roll or possibly two rolls (with one located above the other) when temporally averaged (see Xi & Xia (2008), Weiss & Ahlers (2011) and references therein). The convection rolls in turbulent convection are called large-scale circulation (LSC); it has attracted much attention because it is generally believed to have some connection with (and is statistically similar to) the flow within the Earth's atmosphere (Brown, Nikolaenko & Ahlers 2005*a*). The LSC has many intriguing dynamic features, such as azimuthal rotations and occasional cessations and reversals (Sreenivasan, Bershadski & Niemela 2002; Brown *et al.* 2005*a*; Xi & Xia 2007; Brown & Ahlers 2008*b*). Over the years, the dynamics of LSC has been extensively studied both experimentally and numerically for wide ranges of Ra and Pr in two-dimensional/quasi-two-dimensional systems (Sugiyama *et al.* 2010; Chandra & Verma 2011, 2013; Yanagisawa *et al.* 2011; Ni, Huang & Xia 2015), cubic or box geometries (Wagner & Shishkina 2013; Foroozani *et al.* 2017) and cylindrical cells (Mishra *et al.* 2011; Sakievich, Peet & Adrian 2016; Mamykin *et al.* 2018).

The oscillation of the temperature field (Xi *et al.* 2009) in a cylindrical configuration with unity aspect ratio was found to originate from a sloshing mode at the cell centre (Zhou *et al.* 2009) and a torsional mode near the top and bottom plates (Funfschilling, Brown & Ahlers 2008). Motivated by this discovery, Brown & Ahlers (2008*b*) proposed a stochastic model that could explain the origin of sloshing and torsional oscillations in turbulent convection. This model was subsequently extended by Brown & Ahlers (2008*a*) by including various perturbations that break the rotational invariance of the sample.

An important prediction of this model is the relation between the time-averaged flow strength δ and Re.

Although the results of experiments on LSC in RBC with different geometries (Bai, Ji & Brown 2016; Ji & Brown 2020) and different Pr (Xie, Wei & Xia 2013) are consistent with the predictions from the aforementioned stochastic model, experimental measurements of the LSC strength for low Pr ($Pr < 1$) are still scarce. In experiments at low Pr, compressed gases at ambient temperature ($Pr \sim 1$)(Weiss, Wei & Ahlers 2016), cryogenic helium (Musilová *et al.* 2017) and liquid metal ($Pr \sim 10^{-3}$) (Mamykin *et al.* 2018; Vogt *et al.* 2018) were typically used as the working fluid, and a steel sidewall was used to confine the fluid. However, a steel sidewall has such a large thermal conductivity that embedded thermistors cannot detect the temperature reflecting the LSC. Hence, in the present investigation, we explore the LSC in gaseous RBC with $Pr = 0.72$, and we accomplish this by using a Plexiglas wall.

As Ra increases, an 'ultimate regime' is proposed to exist. In the ultimate regime, the flow is dominated by homogenous turbulence and a turbulent boundary layer. Related to the existence of the ultimate regime is whether a coherent LSC continues to exist at very large Ra, or whether it is totally overwhelmed by fluctuations. To better understand this issue, it is of importance to understand the origin of LSC. Previous studies have discussed whether LSC evolves from the well-known cellular structures at low Ra. On one hand, Krishnamurti & Howard (1981) performed experiments from which they concluded that LSC is not a simple reflection or continuation of the roll structure observed just after the onset of convection. On the other hand, an explicit search for the mode reported by Krishnamurti & Howard (1981) was not successful; see the reviews by Busse (2003) and Hartlep, Tilgner & Busse (2005), who concluded that the LSC at large Ra is indeed a reminder of the structures at low Ra. However, the experiment and simulation in the previously mentioned studies were conducted on RBC samples with a square cross-section, in which the LSC cannot be quantified simply by a temperature measurement, and in Krishnamurti & Howard (1981), shadowgraphs were used to capture the flow structure. In the present work, two RBC samples with a circular cross-section and $\Gamma = 1$ are used, and compressed nitrogen is used as the working fluid. The Ra of the experiment ranges from 10^3 to 10^9, and thus, the flow can be divided into conduction, convection, oscillation, chaotic, transition, and soft and hard turbulent regimes (Threlfall 1975; Heslot, Castaing & Libchaber 1987). Such an Ra range permits us to determine whether the LSC in the turbulent regime evolves from cellular structures in the convection regime.

One advantage of this sample is that in such a geometry, the cellular pattern and the LSC constitute a single roll. Fortunately, the strength and azimuthal orientation of a single roll can be determined by the temperature measured from the wall experimentally (Brown, Funfschilling & Ahlers 2007; Xi & Xia 2008; Xie *et al.* 2013). Hence, in the present study, we focus on a cylindrical sample with unity aspect ratio $\Gamma = 1$ and a finite-conductivity sidewall, which can have a decisive influence on the convective pattern, and we measure the temperature in the wall to directly compare the cellular pattern with the LSC. At small $\Gamma \leqslant 1.6$, the cellular pattern reported by Stork & Müller (1975) and Müller, Neumann & Weber (1984) is an unstable, non-axisymmetric single convection roll corresponding to an azimuthal Fourier mode with $m = 1$. This pattern was further confirmed by Hébert *et al.* (2010), who used the shadowgraph technique and a direct numerical simulation (DNS) to study the aforementioned cellular pattern near the critical Rayleigh number Ra_c. The Ra_c values in cylindrical samples of fairly small Γ have been studied by several theoretical investigations (Charlson & Sani 1970, 1971; Buell & Catton 1983). Among them, only the linear stability analysis extended by Buell & Catton (1983) included the effect of the

finite sidewall conductivity and applied rigid isothermal boundary conditions to the top and bottom of the domain. Moreover, the marginal stability curves were given for several wall admittances $C \equiv [(D/2)\lambda]/(d_w\lambda_w)$, where d_w is the thickness and λ_w is the thermal conductivity of the sidewall. However, the Ra_c for a finite C and $\Gamma = 1$ has not been determined experimentally.

In the present paper, Ra_c is reported to be 7300 for $Pr = 0.72$ and a finite wall admittance $C = 2.02$. In an experiment, the δ values of the cellular pattern and LSC are measured as a function of Ra, revealing a sharp sequence change as a function of Ra. The flow strength of the cellular pattern exhibits sharp growth with Ra in the convection regime, a sudden decrease in the chaotic regime and a further decrease in the transition regime. When Ra is further increased and the RBC evolves into the soft turbulence regime, the LSC becomes self-organised, and the flow strength exhibits sharp growth with Ra. Then, the flow strength decreases as Ra increases in the hard turbulence regime. The dependence of the LSC on Ra is similar to that of the cellular pattern on Ra, suggesting that LSC is an analogy with a cellular pattern. This finding also indicates that the δ of the LSC will further decrease when Ra is larger than that in the present work. Furthermore, a comparison between the present work and previous LSC results for larger Ra and large Pr is made, revealing more sharp changes of the flow strength of the LSC with Ra. Although the flow strength of the LSC is similar to that of the cellular pattern, the preferred orientation of both structures shows a phase difference. In the soft and hard turbulent regimes, Re is also obtained for $Pr = 0.72$, and the result is inconsistent with those of previous studies, and with the prediction from the model by Brown & Ahlers (2008*b*) for $Pr > 3$.

The remainder of this paper is organised as follows. In § 2, we introduce the experimental apparatus, the properties of the fluid used in the experiments and the experimental procedure. In § 3, we present the results regarding the transport of heat and flow strength, we also describe the method used to extract Ra between several regimes, and the Re of the LSC is presented. In § 4, we discuss our results and compare them with those of other experiments. The paper finishes with a brief summary in § 5.

2. Apparatus and procedures

2.1. *The apparatus*

The experiments were conducted with two different sets of convection apparatus, with similar features. The features were described before by Wan *et al.* (2019), but we describe the apparatus in detail here. A schematic diagram is provided in figure 1. From bottom to top, the apparatus consisted first of a bottom adiabatic shield (A) made of aluminium. The central area of the bottom of part A, with a diameter of 25.4 cm, was covered uniformly by parallel straight grooves with a depth of 0.76 cm and a width of 0.40 cm, which were interconnected by semicircles at their ends. Adjacent grooves were separated by a spacing of 1.9 cm. Epoxied into the grooves was a heater made of American Wire Gauge No. 15 nichrome C resistance wire surrounded by fibreglass sleeving.

Suspended above the shield on a steel cylinder 3.8 cm high with a wall thickness of 0.32 cm was the bottom supporting bracket (B) made of aluminium, with a thickness of 3.5 cm. The bottom plate (D) of the sample sat directly above the inner edge of part B. The bottom plate was made of oxygen-free high-conductivity copper with a thickness of 5.08 cm; its top surface was finely machined with tool marks of depth less than 3 μm. The bottom surface was attached to an adhesive film heater (C) (Omega, model KHRA-8/2-P), which had a diameter of 20.3 cm and a resistance of 25.63 Ω. The bottom plate's diameter

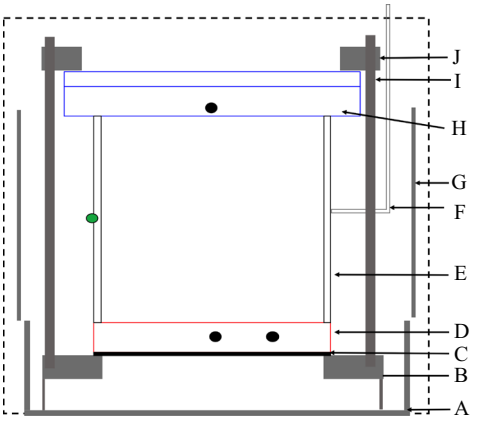

Figure 1. A diagram of an RBC cell. The various parts are explained in the text. The black circles on the top and bottom copper conducting plates represent the embedded thermistors. The green circle in the Plexiglas wall represents a thermistor embedded in a blind hole (without penetrating the wall).

was 22.2 cm, while the central section had a reduced diameter of 20.3 cm and was 0.8 mm thinner than the edge so that the Plexiglas sidewall cylinder (E) was a close sliding fit into the bottom plate. Between parts D and E, an ethylene-propylene O-ring (Parker, model 2-171) was placed in a groove carved into the top surface of the bottom plate; this O-ring prevented the leakage of gas. One small hole was drilled horizontally from the side to the centre of the bottom plate, while a second hole was drilled to $1/2$ of the radius. Thermistors were placed inside a hollow copper tube and embedded into these holes at a vertical distance of 2.53 cm from the top surface of the bottom plate.

The inner diameter D of the Plexiglas sidewalls was measured at several angular and axial positions, and the standard deviation from the measurement mean for a particular sidewall was generally 0.03 cm with a mean D of 19.05 cm. The wall thickness was 0.63 cm. The wall length L was equal to D and was uniform around the circumference to within ± 0.01 cm. A thin Teflon capillary (F) penetrated the sidewall at mid-height and was used to fill the cell. Externally, the capillary was connected to a fill line coming from the gas supply cylinder, to a pressure gauge (Paroscientific Model 745) and to another volume known as the hot volume (HV) (Mueller, Ahlers & Pobell 1976). The HV had a size similar to that of the cell, and its temperature was adjusted in a feedback loop with the pressure gauge to keep the sample pressure constant. The HV is not shown in figure 1.

The sidewall was surrounded by an adiabatic side shield (G) made of aluminium. Epoxied to the outside of this shield was a double spiral of aluminium tubing, through which water from a temperature-controlled circulator flowed. The shield was suspended by six plastic rods above the supporting plate of a rotating table; the supporting plate of the rotating table and the rods are not shown in figure 1. During the measurements, the temperature of the shield was kept close to the mean temperature of the system.

The top of the sample was composed of a copper plate (H) with a diameter of 25.4 cm. This diameter of 25.4 cm was originally designed for the top plate for experimental purposes, as reported by Brown *et al.* (2005*b*). Here, the central section of the top plate was 20.32 cm in diameter and 0.8 mm thinner than the edge. An O-ring was also placed in the groove carved on the bottom surface of the top plate, similar to that in the bottom plate. The top plate had a thickness of 3.34 cm, and a double-spiral water-cooling channel was machined directly into the plate. Small holes were drilled from above through the two-plate

composite to within 0.32 cm of the copper–fluid interface, and calibrated thermistors were mounted into the holes; these thermistors were protected from circulating water by an additional small O-ring between the two plates. In the present work, one thermistor was placed in the centre of the top plate to record the temperature of the top plate. In the top, a retaining aluminium bracket (J) and six tension rods (I) were provided to sustain the force exerted by pressures reaching up to 10 bar. To prevent the convection of air in the vicinity of the sample, the entire space outside the sample, but inside the dashed rectangle K was filled with a low-density (firmness rating 1) polyurethane foam sheet. During the experiment, the whole apparatus was levelled to less than 10^{-4} rad.

2.2. *Temperature measurement*

Two different sidewalls were used in the present work. The first wall (A) had three layers of eight temperature probes embedded in holes on (but not penetrating) the sidewall. The second wall (B) had only one layer of eight temperature probes around the sidewall but six smaller thermistors penetrating the wall into the fluid. In cell A only the temperatures at the mid-height layer were analysed. In cell B only the power spectrum of temperature of one thermistor was analysed. The location of this thermistor was $\xi \equiv (1 - r/(D/2)) = 0.063$ and $z/L = 0.51$, where r is the distance from the axis of the sample and z is the vertical distance from the surface of the bottom plate. In the present work, the side thermistor in cell B was placed around the LSC plane. The Nusselt number, flow strength and Fourier energy were measured mostly from cell A, in which the fluid was not affected by any thermistor. However, with regard to *Re*, the measurement was made from cell B.

Except for those on the sidewalls and inside the fluid, the thermistors used in the apparatus were calibrated simultaneously in a separate apparatus against a laboratory standard based on a standard platinum thermometer. Deviations of the data from the fit were generally less than 0.002 °C. The thermistors were mounted on the adiabatic bottom shield, adiabatic side shield, bottom plate, top plate and bottom aluminium bracket. In contrast, the thermistors embedded on the walls and inside the fluid were calibrated against the top- and bottom-plate thermistors after being installed in the sidewall and inside the fluid. During the calibration, the plate temperatures were set such that $\Delta = 0.1$ °C to ensure that the cell was in equilibrium for more than 12 h. The thermistors in the sidewall and inside the fluid were then assumed to be at the mean temperature T_m of the top and bottom plates. The deviation of the data from the fit was less than 0.01 °C.

2.3. *The fluid*

Nitrogen was used as the working fluid, and nearly all of the measurements were made with a mean temperature of 25.00 °C. Although various physical properties, such as the thermal expansion coefficient α, thermal diffusivity κ and kinematic viscosity ν, depend on the pressure and mean temperature, the nitrogen gas used in the present work yielded a constant *Pr* at different pressures, as demonstrated in figure 2. Another relevant property is the thermal conductivity λ, which gives a value of wall admittance $C \equiv \lambda(D/2)/(\lambda_w d_w)$ (where $\lambda_w = 0.192$ W m^{-1} K is the thermal conductivity of the sidewall and d_w is the thickness of the sidewall). The wall admittance for RBC with nitrogen at 25.00 °C was found to be 2.02.

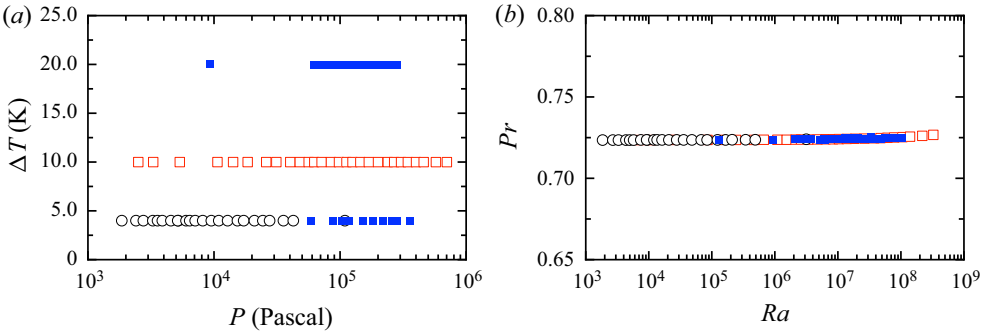

Figure 2. (*a*) A diagram of the gas pressure P and temperature drop Δ between two convection cells. (*b*) A diagram of Pr vs. Ra. In (*a*,*b*), the open symbols represent convection cell A without thermistors disturbing the flow, while the solid symbols represent convection cell B with thermistors inside the fluid.

2.4. *Experimental procedure*

The temperatures of the top and bottom plate were regulated to maintain a constant value at first. Then, the convection cell and the HV were evacuated by a diffusion pump. Nitrogen at a pressure of 10 bar was injected into the convection cell in order to flush the system. Later, the convection cell was re-evacuated. The cell was again flushed with nitrogen to ensure that there were no other gas molecules inside. After being evacuated a third time, the convection cell was filled with nitrogen to a pressure close to the desired value. Then, the valve between the HV and the gas cylinder was closed. The pressure of both the HV and the convection cell was maintained by regulating the temperature of the HV. While the temperature drop and the pressure of the convection cell were maintained at given values, the temperatures of the probes in the convection cell were collected simultaneously. For the next pressure increment, more nitrogen was pumped into the convection cell, and the above procedure was repeated.

During a typical experimental run, at a constant Δ and pressure P, all thermistors were read every 4 s or so for at least 10 h. To evaluate the data, the readings from the first few hours were discarded to avoid transients. Because only the pressure changed slightly between two successive experiments, it was usually sufficient to discard only the first hour of data. In cell B, the thermistors outside the fluid were measured in the same way as the thermistors in cell A. However, each of the six thermistors inside the fluid was connected to an individual multimeter, and data were collected at a rate of 16.6 Hz. In cell B, a given run at equilibrium typically lasted more than 36 h.

3. Results

3.1. *A single-roll structure*

3.1.1. *Quantitative measurements of a single-roll structure*

The strength δ and azimuthal orientation θ_0 of a single-roll structure can be determined by fitting eight temperatures, denoted T_i ($i = 0, \ldots, N_T - 1$, where $N_T = 8$ is the number of thermistors around the sidewall), around the sidewall with the following equation:

$$T_i = T_w + \delta \cos(\theta - \theta_0), \tag{3.1}$$

where T_i denotes the temperature located at azimuthal location θ. Here θ is in the range $-\pi \leqslant \theta < \pi$. Generally, the above equation fits the instantaneous temperature profile well, as shown in figure 3(*a*). However, if the single-roll structure breaks down

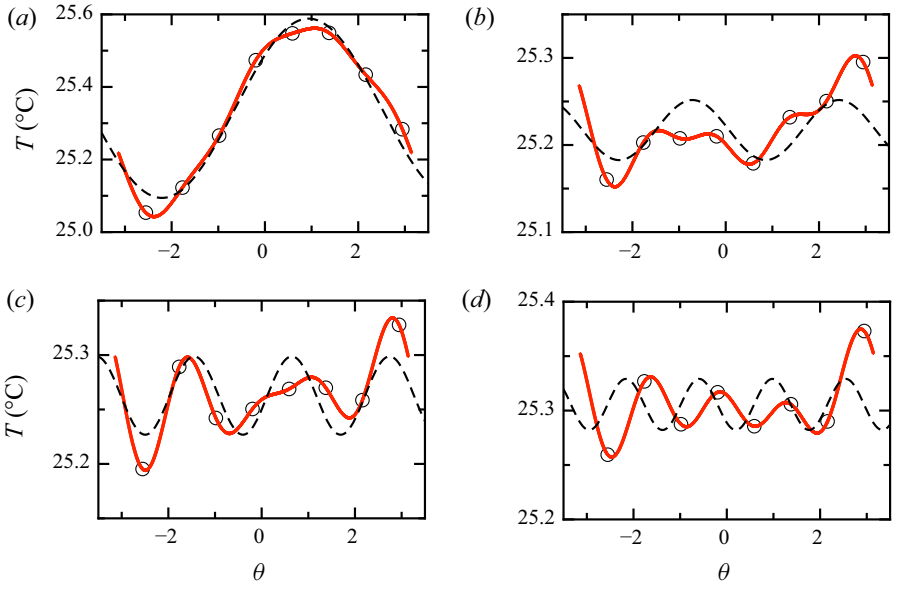

Figure 3. Examples of temperature profiles measured by sidewall thermistors on the mid-height plane. The measurements were taken at $Ra = 6.4 \times 10^6$ and $Pr = 0.72$ in cell A with nitrogen as the working fluid. In (*a*), (*b*), (*c*) and (*d*) the dashed lines represent the fitting by the equation $T = T_w + \cos(m(\theta - \theta_0))$ with $m = 1, 2, 3$ and 4, respectively. The solid lines represent the fitting by (3.2).

and δ is sufficiently small, the above equation does not effectively fit the instantaneous temperatures. As shown in figures 3(*b*), 3(*c*) and 3(*d*) the temperatures are fitted by the equation $T_i = T_w + \delta \cos[m(\theta - \theta_0)]$ with a high mode ($m > 1$, where m represents the number of hot/cold spots evenly appearing on the mid-height plane as visualised from particle image velocimetry by Xi *et al.* 2016). At some Ra, a single-roll structure does not form. To further quantify the flow structure and make use of all eight temperatures, we computed the coefficients for the lowest four Fourier modes from the N_T temperatures T_i as follows:

$$T_i = \sum_{m=0}^{N_T/2} A_m \cos(m\theta) + B_m \sin(m\theta). \tag{3.2}$$

The above yielded all eight Fourier coefficients A_m (the cosine coefficients) and B_m (the sine coefficients), $m = 1, \ldots, 4$, for the case where there are eight temperatures. From these coefficients, we determined the energy $E_m = A_m^2 + B_m^2$ for each mode $m = 1, \ldots, N_T/2$. Then, the first Fourier energy mode is $E_1 = \delta^2$, and the orientation of the single-roll structure is given by $\theta = \arctan(B_1/A_1)$. If the flow structure is a single roll and the horizontal mid-height plane consists of only one hot up-flow and one cold down-flow, (3.1) will apparently fit the temperatures well as shown in figure 3(*a*), and the ratio E_1/E_{tot} should be close to 1. However, when the single-roll structure breaks down, the ratio E_1/E_{tot} vanishes. As shown in figure 3(*b*), at the dominant higher Fourier energy mode ($m = 2$), the Fourier energy ratio E_2/E_{tot} is much larger than that at the other modes. Higher modes $m = 3$ and $m = 4$ are dominant in figures 3(*c*) and 3(*d*), respectively. Table 1 also lists the total energy and the ratio of each energy mode, in total energy, for the examples in figure 3. The examples are all taken for $Ra = 6.4 \times 10^6$ and $\Delta = 10.0$ K, but

Case	E_{tot}	E_1/E_{tot}	E_2/E_{tot}	E_3/E_{tot}	E_4/E_{tot}
Figure 3(a)	0.063	0.976	0.017	0.003	0.004
Figure 3(b)	0.003	0.352	0.426	0.109	0.114
Figure 3(c)	0.002	0.101	0.051	0.624	0.224
Figure 3(d)	0.001	0.069	0.189	0.307	0.436

Table 1. The total Fourier energy E_{tot}, and the ratio of Fourier energy and total energy E_m/E_{tot} ($m = 1, \ldots, 4$) for the examples in figure 3.

the total Fourier energy in figures 3(b), 3(c) and 3(d) are much smaller than figure 3(a). In figures 3(b), 3(c) and 3(d) the ratio of the first energy mode are all smaller than 0.4.

Next, we examined how the Fourier mode describes the dynamics of the single-roll structure. In figures 4, 5, 6, 7, 8 and 9 the time trace of temperature measured from the sidewall, the corresponding Fourier energy, the flow strength and orientation are plotted for different Ra. Apparently the total Fourier energy gives a similar trend as the flow strength for most of Ra. When Ra is large enough, the flow strength varies drastically as time changes. In turbulent RBC, at a given Ra the LSC strength $\delta \sim 0$ corresponds to a process called cessation, during which the LSC breaks down owing to the strong stochastic turbulent background. If the flow strength $\delta < \beta\langle\delta\rangle$, cessation occurs. However, the selection of β is quite arbitrary in the previous literature. Furthermore, the aforementioned criteria for cessation are not applicable when cessation is the most common state of flow and the time-averaged flow strength $\langle\delta\rangle$ is nearly 0, as shown in figure 7 for $Ra = 6.4 \times 10^6$. Here, we proposed that $E_1/E_{tot} < 0.4$ can be used as the criterion of cessation. In figure 8(e), the minimum value of the first energy mode takes up more than 0.4 total energy, therefore there is no cessation at this Ra. Using the ratio E_m/E_{tot}, it is easier to determine the order of the mode dominating the flow that breaks down the single-roll structure. To better illustrate this technique, the time traces of E_{tot} and each ratio E_m/E_{tot} were also plotted in figure 7(c,d). At $Ra = 6.4 \times 10^6$, the flow structure does not form even a single roll, as E_1/E_{tot} is mainly less than 0.5. Surprisingly, the dominant Fourier mode at this Ra is $m = 4$, whose energy takes up to more than half of the total Fourier energy. In a later section, the time-averaged values and standard deviations of the flow strength δ and orientation θ_0 will be analysed in addition to the ratio of each Fourier mode E_m/E_{tot} ($m = 1, \ldots, 4$).

3.1.2. *Convective pattern and large-scale circulation*

We first examined the Rayleigh number range where the cellular pattern and the LSC exist separately. Figure 10(a) shows plots of the flow strength $\langle\delta\rangle/\Delta$ as a function of Ra with $Pr = 0.72$ and nitrogen as the working fluid. Obviously, the data show a sequence of discontinuities. By fitting the data with several logarithmic functions, the transitions between six regimes are determined (except the oscillation regime, which is determined by the power spectrum of the temperature embedded in the sidewall). These seven regimes, namely, conduction, convection, oscillation, chaotic, transition, soft turbulence and hard turbulence, are consistent with those reported by Heslot *et al.* (1987). In the present case, the Ra of the transitions between these seven different regimes are denoted Ra_c, Ra_o, Ra_{ch}, Ra_{tr}, Ra_s and Ra_h with values of 7300, 1.35×10^5, 1.65×10^5, 6.14×10^5, 8.38×10^6 and 9.18×10^7, respectively. Hence, the Ra between the transitions can also be expressed as $Ra_o = 18.5Ra_c$, $Ra_{ch} = 22.6Ra_c$, $Ra_{tr} = 84Ra_c$, $Ra_s = 1148Ra_c$, $Ra_h = 12\,575Ra_c$.

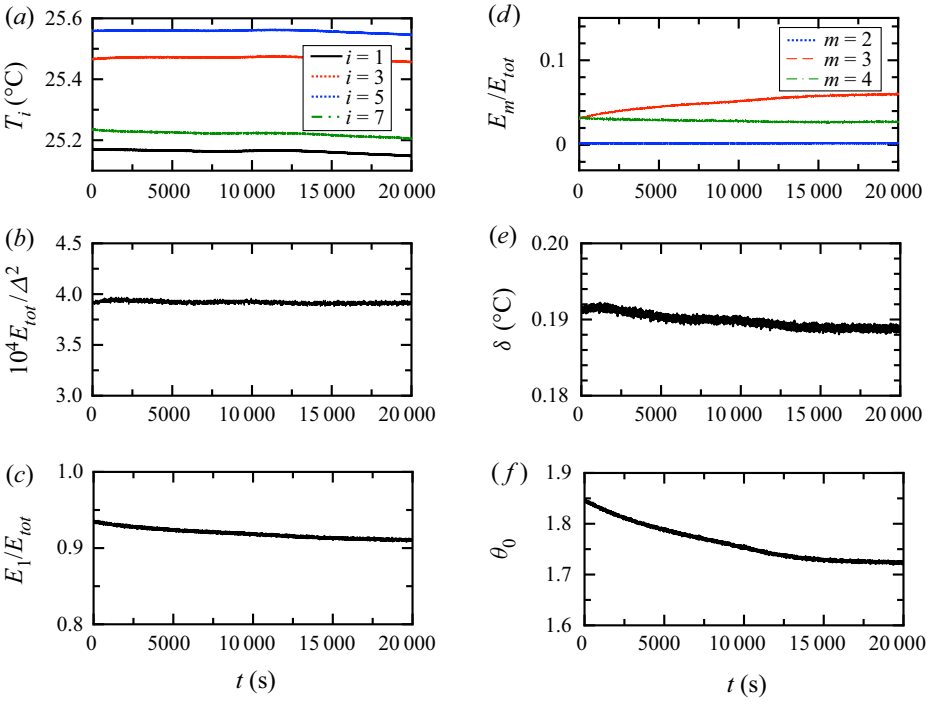

Figure 4. The time trace of various quantities for convection regime with $Ra = 8.5 \times 10^4$. (*a*) The four temperatures measured at mid-height. (*b*) The total Fourier energy $10^4 E_{tot}/\Delta^2$. (*c*) The ratio of the first Fourier energy mode and total energy E_1/E_{tot}. (*d*) The ratio E_m/E_{tot} with $m = 2$, 3 and 4. (*e*) The flow strength δ. (*f*) The LSC orientation θ.

In the conduction regime, $\langle\delta\rangle/\Delta$ has a value of 0.0047, close to but still greater than 0. This measurement was taken at $\Delta = 4.00$ K, so it yields a temperature difference of nearly 20 mK, which is only twice the measurement error. Thus, we consider this as the measurement error. As Ra is increased beyond Ra_c, the strength of the cellular pattern sharply increases and reaches a maximum 0.02 in the convection regime. A sharp increase in cellular strength was also observed by Hébert *et al.* (2010), who used the shadowgraph image variance σ^2 to determine Ra_c. Those authors found that σ^2 experiences linear growth with Ra when Ra is just greater than Ra_c, a similar trend to that of the Nusselt number. Therefore, we also expected a linear increase in $\langle\delta\rangle/\Delta$ with $Ra^{1/2}$ because the first Fourier energy is δ^2 as mentioned previously. Although we obtained only a few data points at the onset of convection, they are sufficient to fit function $\langle\delta/\Delta\rangle = k(Ra - Ra_c)^{1/2} + b$ to obtain $Ra_c = 7300$. We note that the Ra_c value determined by a logarithmic function is close to 7300 in figure 18 in Appendix A.

The oscillation regime cannot be determined from the relation between the flow strength and Ra, so we will discuss the oscillation regime in a later section. As Ra increases up to Ra_{ch}, the strength of a single roll varies over time. From figure 10(*b*), we can see that the fluctuation in the flow strength increases as Ra is increased in the chaotic regime. However, the flow with the $m = 1$ mode is still dominant in the chaotic regime, as shown in figure 11. The energy ratio $E_1/E_{tot} > 0.75$ means that the flow always forms a single roll in the cell. This single-roll flow usually meanders around a preferred orientation, as shown in figure 12, where the time-averaged orientation $\langle\theta\rangle \sim 2$ rad, but the fluctuation in the orientation σ_θ is approximately 0.15 rad. In the transition regime $Ra > Ra_{tr}$, the

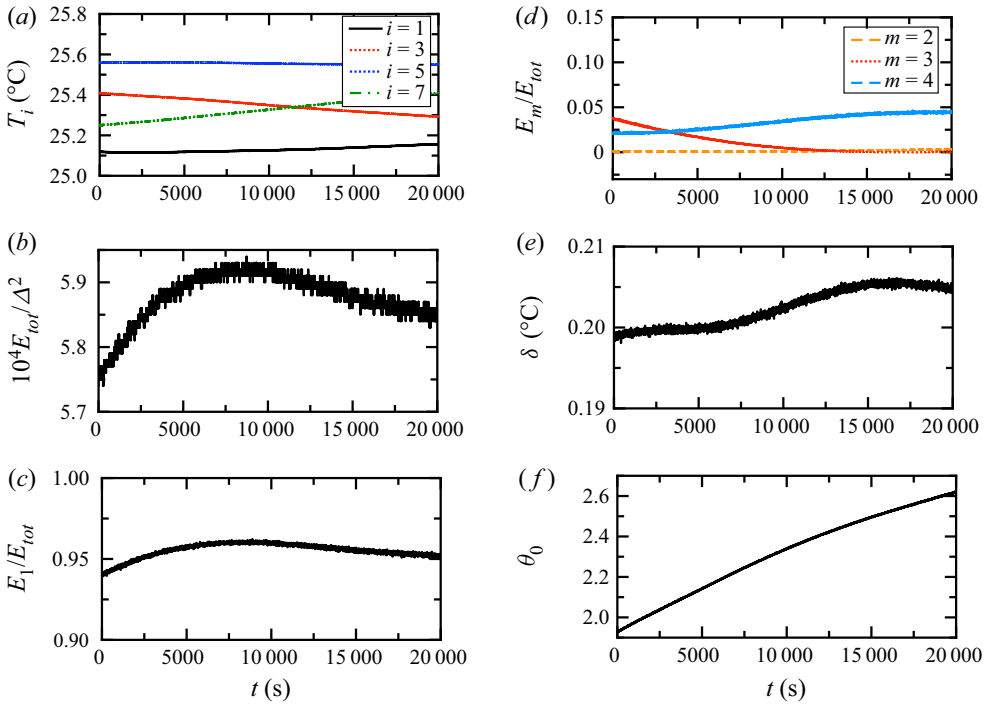

Figure 5. The time trace of various quantities for oscillation regime with $Ra = 1.5 \times 10^5$. (*a*) The four temperatures measured at mid-height. (*b*) The total Fourier energy $10^4 E_{tot}/\Delta^2$. (*c*) The ratio of the first Fourier energy mode and total energy E_1/E_{tot}. (*d*) The ratio E_m/E_{tot} with $m = 2$, 3 and 4. (*e*) The flow strength δ. (*f*) The LSC orientation θ.

time-averaged flow strength continues to decrease to the value in the conduction regime, which represents the resolution of the experimental measurement. For a given Ra, the flow strength of the single-roll structure varies temporally, as demonstrated in figures 4, 6, 7, 8 and 9. To ascertain whether the single-roll flow retains its shape, the time trace of the ratio E_m/E_{tot} in transition regime is also plotted in figure 7(*c*), indicating that the single-roll flow breaks down and then reforms itself during the measurement period. When the $m = 1$ single-roll flow vanishes, the strong background fluctuation represented by the $m = 4$ mode in the present measurement is dominant. In the transition regime, the ratio E_4/E_{tot} is comparable with E_1/E_{tot}. Another difference between the chaotic and transition regimes also lies in the correlation between the temperature in the centre and the temperature near the sidewall; this correlation is not shown in the present work because it is consistent with the previous measurements by Heslot *et al.* (1987). In the chaotic regime, the temperatures in the centre and near the sidewall are strongly correlated. Once the flow changes to the transition regime, this correlation disappears.

As Ra is further increased to the soft turbulence regime, a single-roll LSC is observed. As Ra increases, the time-averaged flow strength $\langle\delta\rangle/\Delta$ increases sharply, but the standard deviation of the flow strength σ_δ/Δ also decreases drastically. The maximum LSC strength is 50 % larger than the maximum value of the cellular pattern strength. The corresponding onset of turbulence at $Ra_s = 8.38 \times 10^6$ was determined from fitting a logarithmic function to the time-averaged flow strength $\langle\delta\rangle/\Delta$ against Ra. However, if the time-averaged flow strength is fitted by the function $\langle\delta/\Delta\rangle = k(Ra - Ra_s)^{1/2} + b$, the value of Ra_s is still close to 8.38×10^6, as shown in figure 18 in Appendix A.

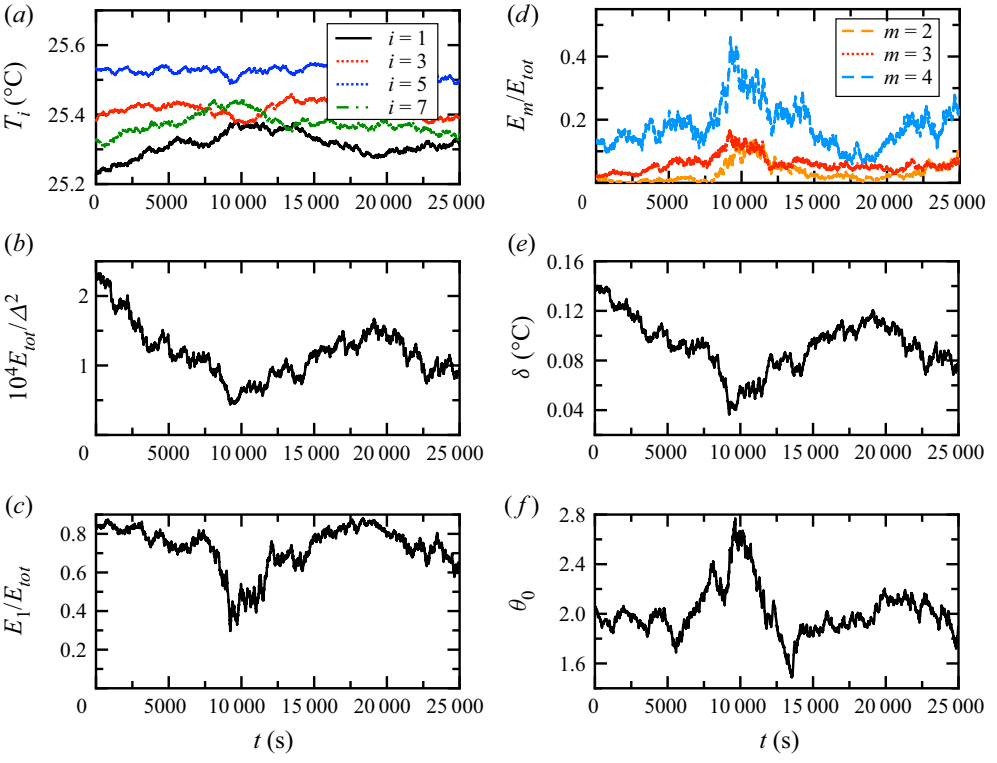

Figure 6. The time trace of various quantities for the chaotic regime with $Ra = 4.7 \times 10^5$. (*a*) The four temperatures measured at mid-height. (*b*) The total Fourier energy $10^4 E_{tot}/\Delta^2$. (*c*) The ratio of the first Fourier energy mode and total energy E_1/E_{tot}. (*d*) The ratio E_m/E_{tot} with $m = 2$, 3 and 4. (*e*) The flow strength δ. (*f*) The LSC orientation θ.

Interestingly, the single-roll LSC is stronger under a more turbulent background, which is represented by *Ra*. However, in the hard turbulence regime, the strength of the LSC decreases as *Ra* increases and the turbulent background becomes stronger. In hard turbulence where $Ra > Ra_h$, the flow strength $\langle\delta\rangle/\Delta$ slowly decreases as *Ra* increases, and the standard deviation of the flow strength σ_δ is close to 0, which means that the strength of the LSC is barely affected by the turbulent background.

The growth of the LSC strength with *Ra* is similar to that of the cellular pattern, suggesting that the LSC reflects low *Ra* structures. However, some interesting differences remain between the cellular pattern and the LSC, as shown in figure 12. It is well known that the single-roll LSC meanders randomly around a preferred orientation θ_m, which would be apparent in the probability distribution of the orientation $p(\theta_0)$ given sufficient statistical data. However, in present work the measurement of LSC in equilibrium for each *Ra* only lasts for approximately 8 h, and it is difficult to determine the peak at the probability density function (p.d.f.) of θ_0 as shown in figure 13(*f*) for $Ra = 1.1 \times 10^8$. So here we take the time-averaged orientation $\langle\theta_0\rangle$ as a preferred orientation; θ_0 would ideally be uniformly distributed in an azimuthally symmetric system, but minor deviations from perfect rotational symmetry such as a slightly elliptical cross-section of the sidewall, a systematic temperature gradient in the top plate owing to the cooling system or a coupling of the Earth's Coriolis force to the LSC (Brown & Ahlers 2006) could cause a deviation from the uniform distribution. It is worth noting that the orientation of the cellular pattern

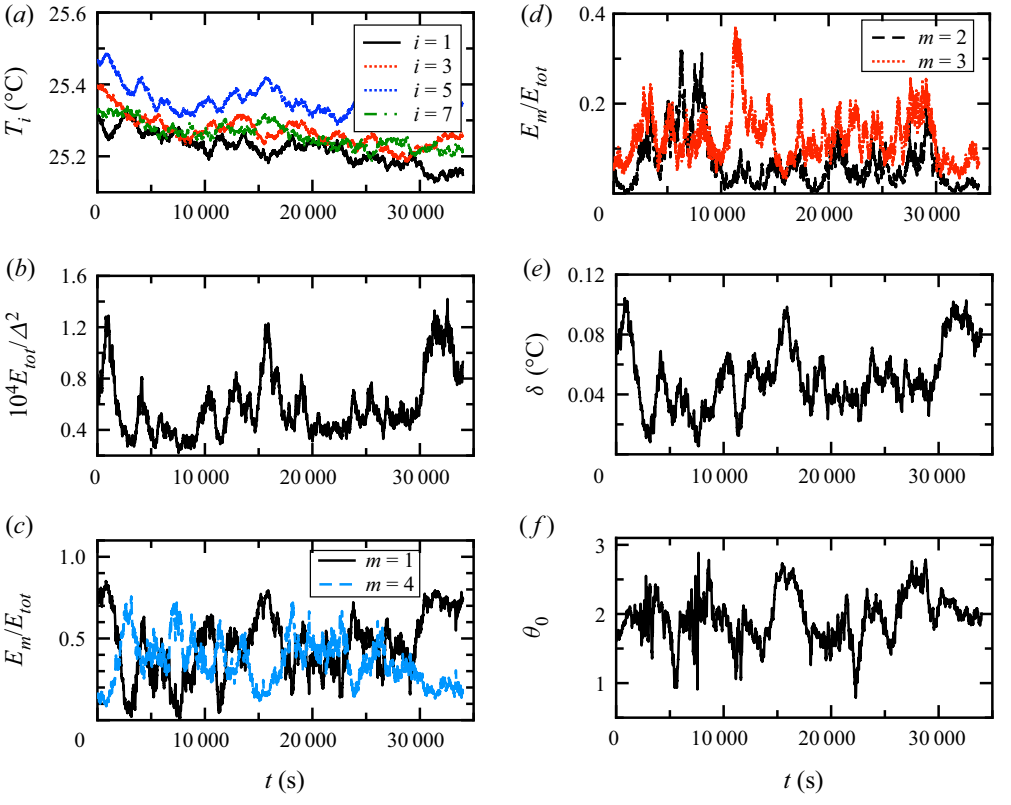

Figure 7. The time trace of various quantities for the transition regime with $Ra = 6.4 \times 10^6$. (*a*) The four temperatures measured at mid-height. (*b*) The total Fourier energy $10^4 E_{tot}/\Delta^2$. (*c*) The ratio of the first Fourier energy mode and total energy E_1/E_{tot}. (*d*) The ratio E_m/E_{tot} with $m = 2$, 3 and 4. (*e*) The flow strength δ. (*f*) The LSC orientation θ.

has a phase difference of approximately $\pi/4$ from that of the LSC. In the soft turbulence regime, the relation of $\langle\theta\rangle$ against *Ra* shows a smooth change in the flow orientation. In figure 13, the distribution of the orientations are plotted for different *Ra*. In the convection regime, the pattern stays at the orientation about $\theta = 2$. In the oscillation regime, the pattern slowly moves in clockwise direction to the orientation 2.6 in figure 5(*f*). In the chaotic and transition regimes, the pattern varies over the plates at a range $0.5 < \theta < 3$. In the soft turbulence regime, the LSC meanders about a preferred orientation, and this orientation is smaller with increasing *Ra*. In the hard turbulence regime, the preferred orientation of LSC varies little as *Ra* increases. In convection cell A, the cell was levelled within the error of measurement, and the capillary tube was oriented east, which is the preferred orientation of the LSC. If the preferred orientation of the LSC suggests that an imperfect element oriented east was introduced during the experiment, we are surprised to find that the cellular pattern chooses to be $\pi/4$ away from that imperfect element. More studies comparing cellular patterns with LSC are needed to shed light on this phenomenon.

3.2. *Reynolds numbers based on the turnover time of large-scale convection*

Another difference between cellular patterns and the LSC is that the latter can be described by a unique eddy-turnover time in turbulent context, which is correlated with the

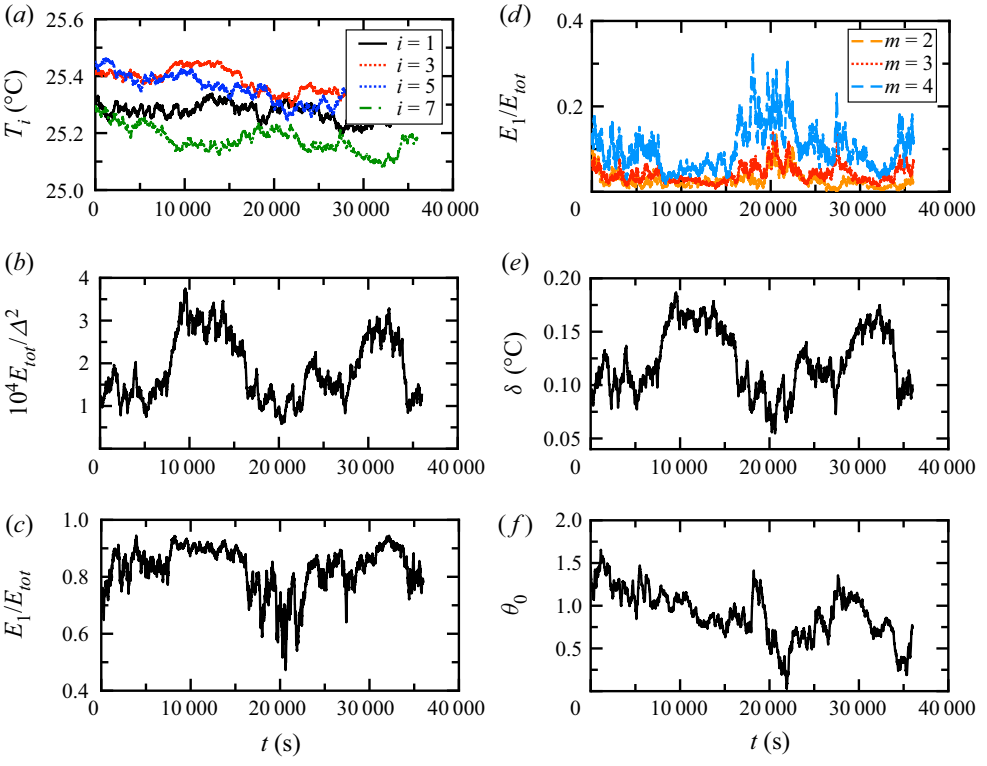

Figure 8. The time trace of various quantities for the soft turbulence regime with $Ra = 1.4 \times 10^7$. (*a*) The four temperatures measured at mid-height. (*b*) The total Fourier energy $10^4 E_{tot}/\Delta^2$. (*c*) The ratio of the first Fourier energy mode and total energy E_1/E_{tot}. (*d*) The ratio E_m/E_{tot} with $m = 2$, 3 and 4. (*e*) The flow strength δ. (*f*) The LSC orientation θ.

oscillation period τ_0 of the LSC. The oscillation period τ_0 was inferred as the oscillation time from the autocorrelation of a single temperature measurement. From the temperature power spectra shown in figure 14, the frequency of the peak f_0 is equivalent to $1/\tau_0$. Therefore, using L as a relevant length scale, Re can be defined as

$$Re \equiv \frac{2L^2 f_0}{\nu}. \tag{3.3}$$

In cell A, the temperatures in the sidewall (except in the oscillation regime) do not show obvious peaks in the temperature power spectra, mainly because the Plexiglas wall used in the present work is twice as thick as the wall used in Brown *et al.* (2007). Hence, the oscillation of the temperature owing to the LSC is damped before it is detected by the probe. In convection cell B, which has thermistors inside the fluid, only the power spectra in the soft and hard turbulence regimes show obvious peaks, as indicated in figure 14(*a*). Because the thermistor near the sidewall inside the fluid is located on the LSC plane, the oscillation peak of the side temperature represents the turnover time of the LSC (Brown *et al.* 2007).

The LSC turnover time has been studied extensively in a large range of both Ra and Pr. For comparison purposes, figure 15 plots our data with those from two other experiments. One set of data is Re^{pl}, which is also based on the LSC turnover time of Brown & Ahlers (2007) and is taken from RBC with $\Gamma = 1.00$ and $Pr = 3.32$, 4.38 and 5.55. The other set

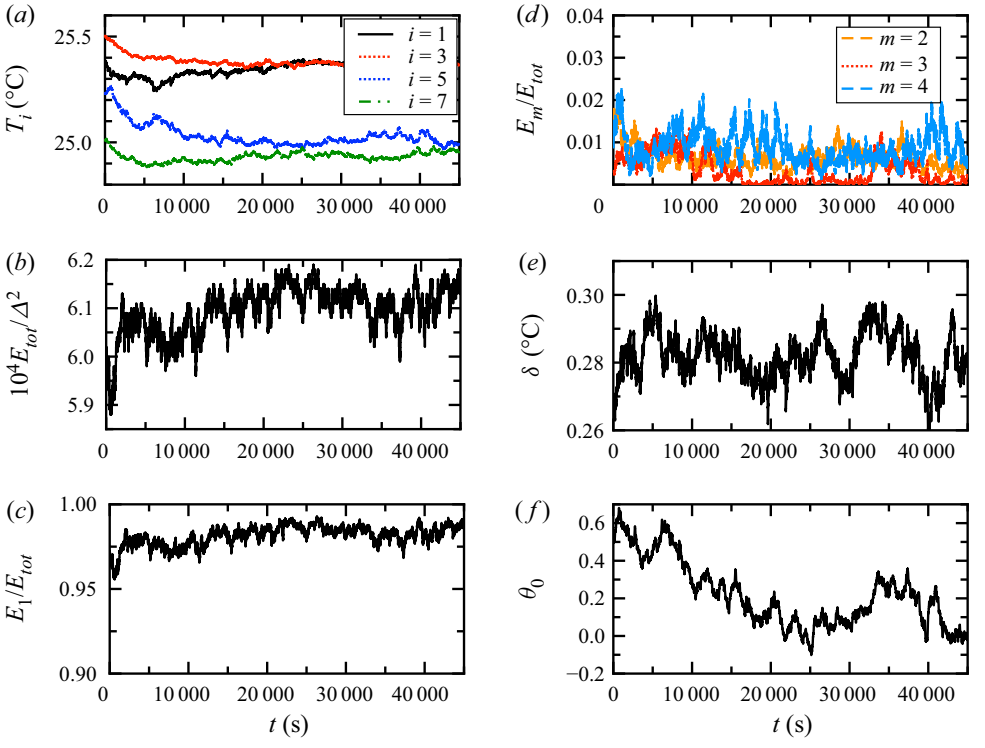

Figure 9. The time trace of various quantities for the hard turbulence regime with $Ra = 1.1 \times 10^8$. (*a*) The four temperatures measured at mid-height. (*b*) The total Fourier energy $10^4 E_{tot}/\Delta^2$. (*c*) The ratio of the first Fourier energy mode and total energy E_1/E_{tot}. (*d*) The ratio E_m/E_{tot} with $m = 2$, 3 and 4. (*e*) The flow strength δ. (*f*) The LSC orientation θ.

is run 'C' of Bruno convection taken from RBC with unity Γ using cryogenic helium gas as the working fluid, yielding $Pr \sim 1$. The Pr of the experiment with cryogenic helium gas from Musilová *et al.* (2017) is close to our Pr, but there is a discrepancy between the Re_{f_0} of our work and that measured with cryogenic helium gas. Figure 15(*a*) also demonstrates that our LSC turnover time is consistent with that of Brown & Ahlers (2007), who employed a larger Pr than ours.

Brown & Ahlers (2008*b*) proposed a model consisting of two stochastic ordinary differential equations to explain most of the features of LSC dynamics. One important prediction of this model is the relation between the normalised flow strength of the LSC and Re, which is expressed as

$$\frac{\langle\delta\rangle}{\Delta} \times \frac{Ra}{Pr} = 18\pi Re^{3/2}. \tag{3.4}$$

However, the experimental data obtained by Brown & Ahlers (2008*b*) from RBC with $Pr = 3.3$, 4.4 and 5.5 yield $\langle\delta\rangle/\Delta \times Ra/Pr = 159Re^{3/2}$, the coefficient of which is 2.8 times greater than the predicted value of 18π. For comparison, we plot our results obtained from cell B with the LSC model in figure 16. In cell B, the LSC strength δ is also determined from the temperature in the sidewall, as described before. Figure 17 reveals that the LSC strength $\langle\delta\rangle/\Delta$ in cell B for the turbulence regime is overall larger than that in cell A by a value independent of Ra because the LSC in cell B is under the influence of thermistors penetrating the wall into fluid. However, we assume that the relation between

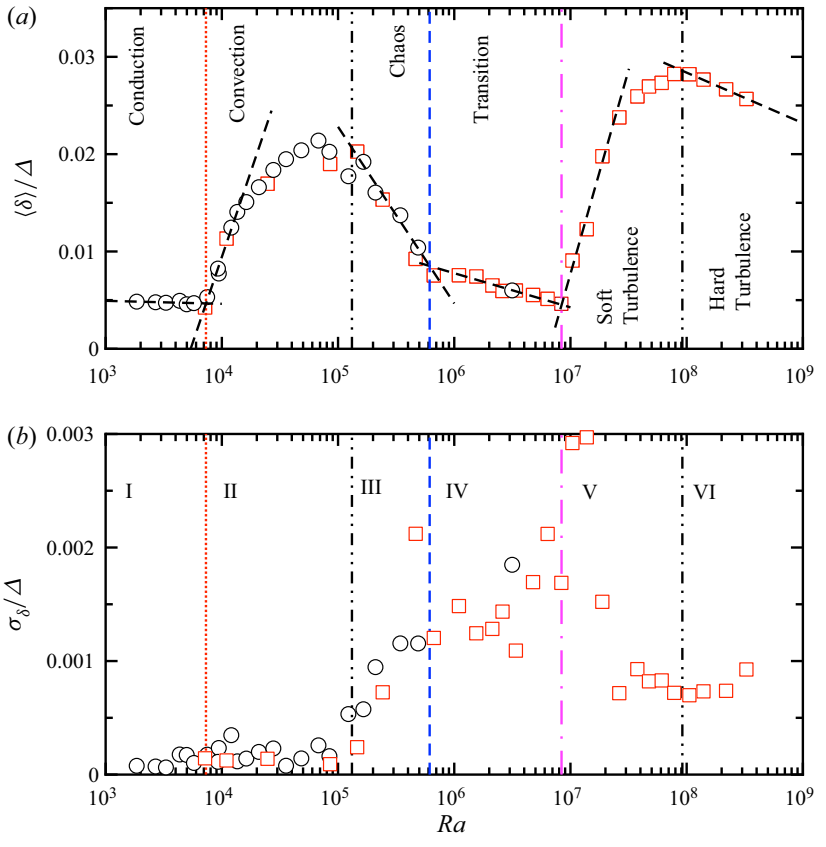

Figure 10. Plots of (*a*) the single-roll flow strength $\langle\delta\rangle/\Delta$ and (*b*) σ_δ/Δ against Ra for cell A. Six dynamical states are labelled. From left to right, they are (I) convection, (II) conduction, (III) chaotic, (IV) transition, (V) soft turbulence and (VI) hard turbulence. The dashed lines are logarithmic function fits to various segments of data serving as visual guides. The vertical lines from left to right are as follows: $Ra_c = 7300$, $Ra_{ch} = 1.85 \times 10^5$, $Ra_{tr} = 6.14 \times 10^5$, $Ra_s = 8.38 \times 10^6$ and $Ra_h = 9.18 \times 10^7$. (Here, the oscillation regime between the corresponding $Ra_o = 1.35 \times 10^5$ and Ra_{ch} is not shown.) The measurements were taken from cell A for $\Delta = 4.00$ K (black circles) and $\Delta = 10.00$ K (red squares).

the LSC strength and Re is the same in both cells. Figure 16 demonstrates that our data can be fitted with two power laws: $\langle\delta\rangle/\Delta \times Ra/Pr = 0.007Re^{3.0\pm0.6}$ for $Re < 400$ and $\langle\delta\rangle/\Delta \times Ra/Pr = 15.4Re^{1.76\pm0.06}$ for $Re > 400$. Interestingly, the data fitted by the second line are between the theoretical prediction and the experimental result of Brown & Ahlers (2008*b*).

In the present work, the oscillation regime can be identified only for $Ra = 1.35 \times 10^5$ and 1.65×10^5. It is difficult to see the oscillation regime from the time trace of any temperature measurement in the wall, but this regime can be found from the power spectra of the temperature measured in the sidewall in figure 14(*a*), an obvious peak at the oscillation frequency f_0 can be identified. Here, the values of f_0 were found to be 0.061 and 0.038 Hz for $Ra = 1.46 \times 10^5$ with $\Delta = 10.00$ K and 1.65×10^5 with $\Delta = 4.00$ K. To compare our oscillation frequency with the oscillation frequency of the LSC corresponding to the LSC turnover frequency in the turbulence regime, we employed the dimensionless Re based on the oscillation frequency in (3.3). Values of $Re = 41.08$ and 43.91 were obtained for $Ra = 1.46 \times 10^5$ with $\Delta = 10.00$ K and 1.65×10^5 with

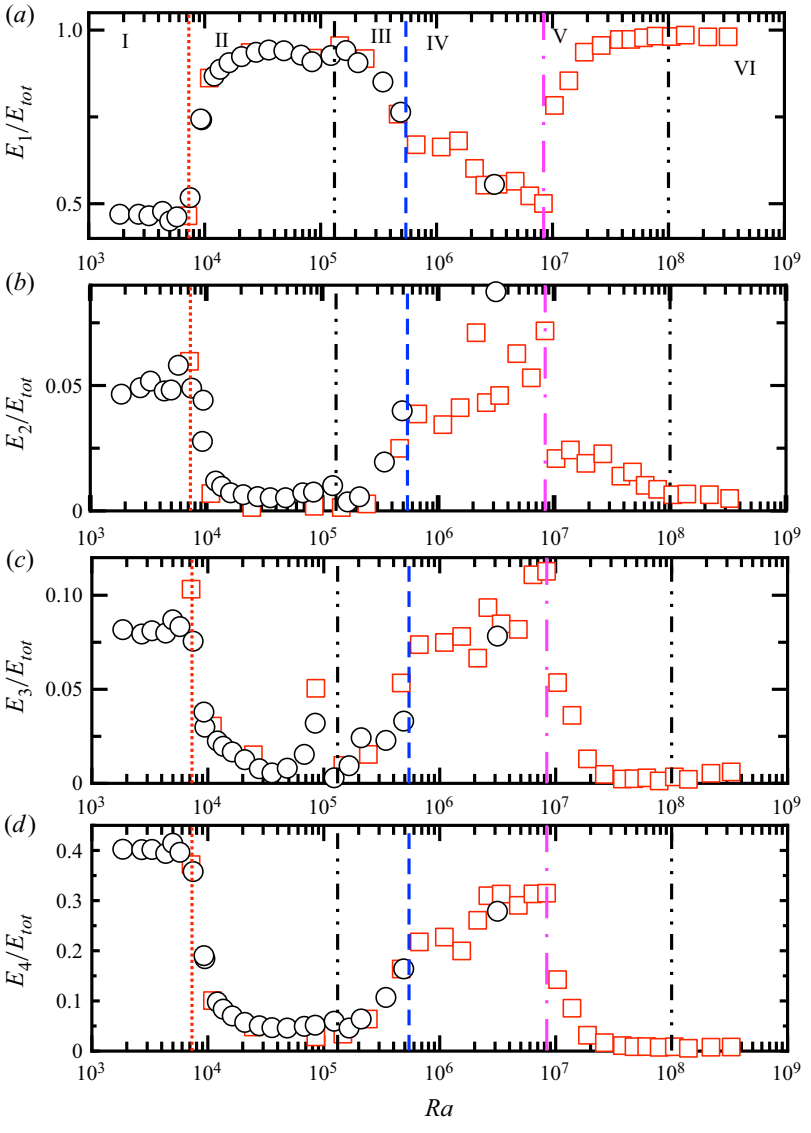

Figure 11. The ratios of the mth mode of Fourier energy to the total Fourier energy E_m/E_{tot} ($m = 1, \ldots, 4$) against Ra. The vertical lines represent the transitions between different dynamic regimes. The measurements were taken from cell A for $\Delta = 4.00$ K (black circles) and $\Delta = 10.00$ K (red squares).

$\Delta = 4.00$ K. The compensated quantities $ReRa^{-1/2}$ are 0.1075 and 0.1081. We plot $ReRa^{-1/2}Pr^{0.62}$ for these two Ra values as a dashed line in figure 15(b). Surprisingly, the results are consistent with those for larger Pr.

4. Discussion

Our results suggest that LSC is an analogy to low Ra structures. The trend of the LSC flow strength as Ra varies under turbulence is similar to the trend of the cellular pattern in the convection and chaotic regimes. One might expect that the LSC strength at larger Ra (far beyond hard turbulence) shows a decrease with increasing Ra similar to that

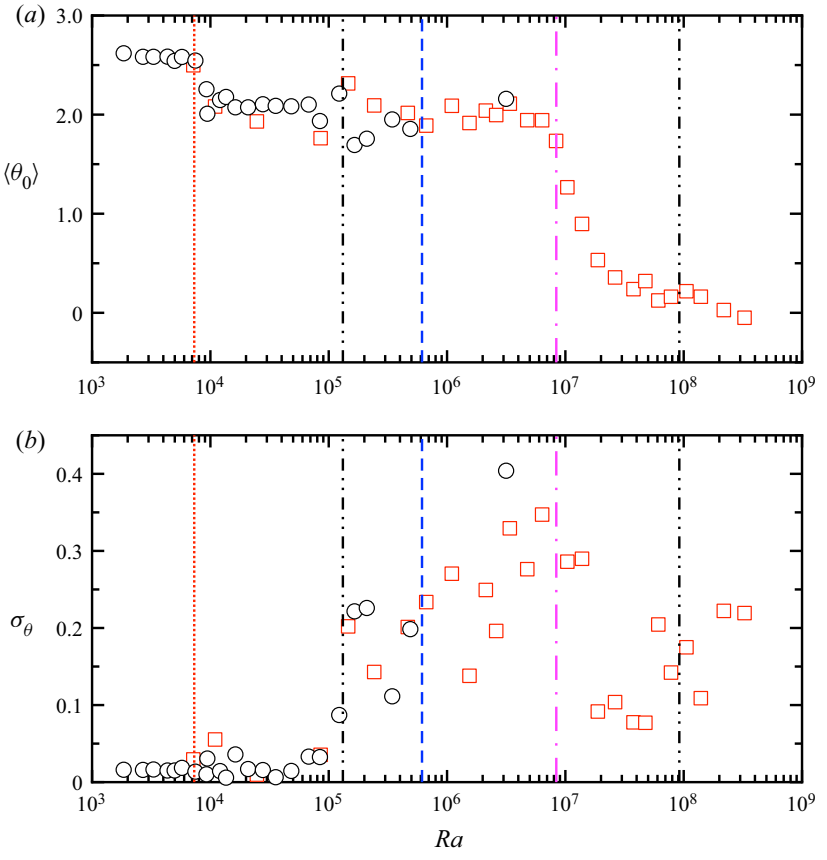

Figure 12. (*a*) The time-averaged orientation $\langle\theta\rangle$ and (*b*) the standard deviation σ_θ of the LSC against *Ra*. The vertical lines represent the transitions between different dynamic regimes. The measurements were taken from cell A for $\Delta = 4.00$ K (black circles) and $\Delta = 10.00$ K (red squares).

in the transition regime. Therefore, we plot our data and the LSC strength of Brown & Ahlers (2007) with $Pr = 4.38$ and $3 \times 10^9 < Ra < 2 \times 10^{10}$ in figure 17. The LSC strength with $Pr = 12.3$ and $6 \times 10^{10} < Ra < 6 \times 10^{11}$ of Wei & Ahlers (2016) and the $\langle\delta\rangle/\Delta$ with $Pr \sim 0.7$ and $10^{12} < Ra < 2 \times 10^{14}$ of He, Bodenschatz & Ahlers (2016) are also plotted for comparison. In Brown & Ahlers (2007), the data were fitted by the power law $21Ra^{-0.32}$. Here, we plot the data on a semi-logarithmic scale because the difference in $\langle\delta\rangle/\Delta$ can be illustrated better this way. Clearly, the trend of the flow strength as *Ra* varies at large *Ra* in the hard turbulence regime is similar to the trends in the chaotic and transition regimes. The transition between the two lines in figure 17 is 4×10^9, which is close to the value reported in Brown & Ahlers (2007), beyond which the twisting motion and the *Re* value based on the turnover time show discrepancies. For $Ra \leqslant 3 \times 10^9$, the experimental results of Brown & Ahlers (2007) and Xi, Zhou & Xia (2006) suggest the existence of a new LSC state in which the plumes and the LSC are no longer slaved to each other and where the twist oscillation of the LSC is no longer synchronous with the LSC turnover time. For $Ra > 3 \times 10^{11}$, the data with $Pr = 12.3$ in figure 17 show another transition, but confirming this phenomenon requires more measurements at larger *Ra* and $Pr > 1$. When *Ra* is further increased, the data of He *et al.* (2016) show that a statistically well defined, albeit highly fluctuating single-roll LSC still exists in both the classic regime

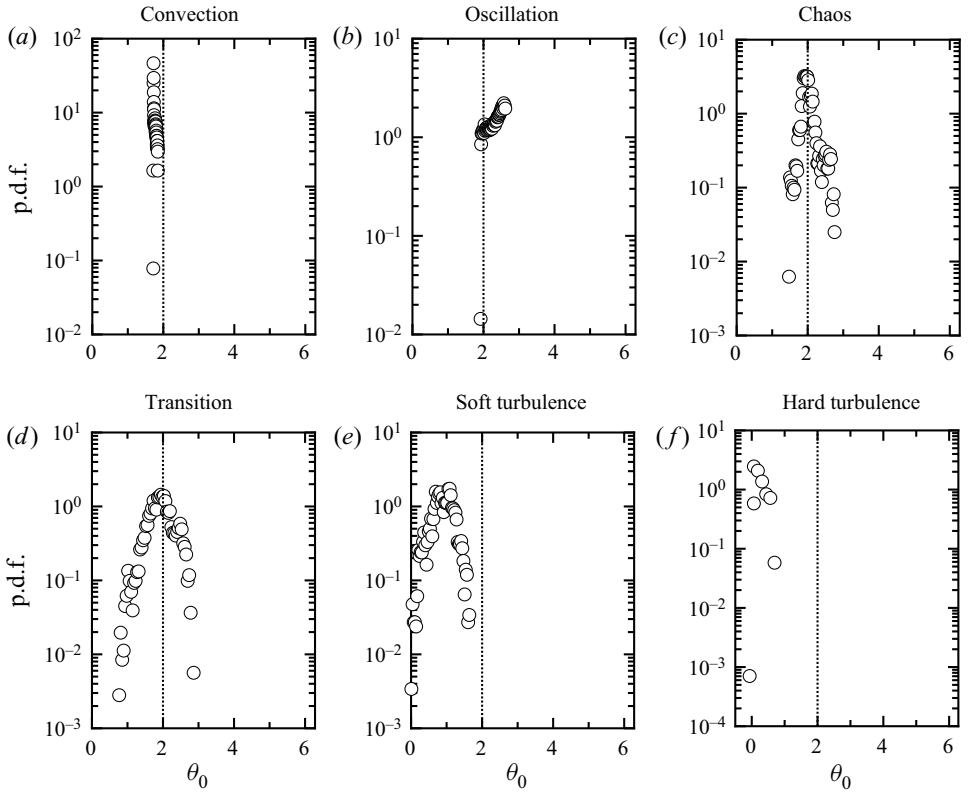

Figure 13. The p.d.f. distribution of the LSC orientation θ for various regimes. (*a*) Convection regime with $Ra = 8.5 \times 10^4$. (*b*) Oscillation regime with $Ra = 1.5 \times 10^5$. (*c*) Chaotic regime with $Ra = 4.7 \times 10^5$. (*d*) Transition regime with $Ra = 6.4 \times 10^6$. (*e*) Soft turbulence regime with $Ra = 1.4 \times 10^7$. (*f*) Hard turbulence regime with $Ra = 1.1 \times 10^8$. The vertical lines represent the azimuthal location $\theta = 2.0$. The measurements were taken from cell A.

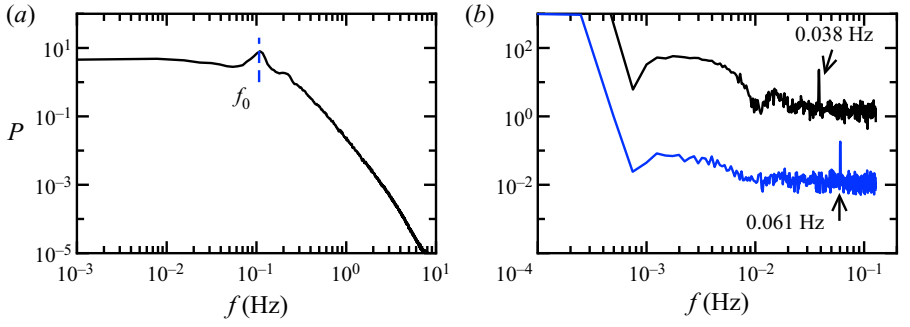

Figure 14. (*a*) The temperature power spectra located at $\xi = 0.063$ and $z/L = 0.51$ inside fluid of cell B for $Ra = 7.75 \times 10^7$ (soft turbulence). (*b*) From bottom to top, the temperature power spectrum located at $\pi/16$ in the sidewall of cell A for $Ra = 1.35 \times 10^5$ with $\Delta = 10$ K and for $Ra = 1.65 \times 10^5$ with $\Delta = 4$ K; both Ra are in the oscillation regime.

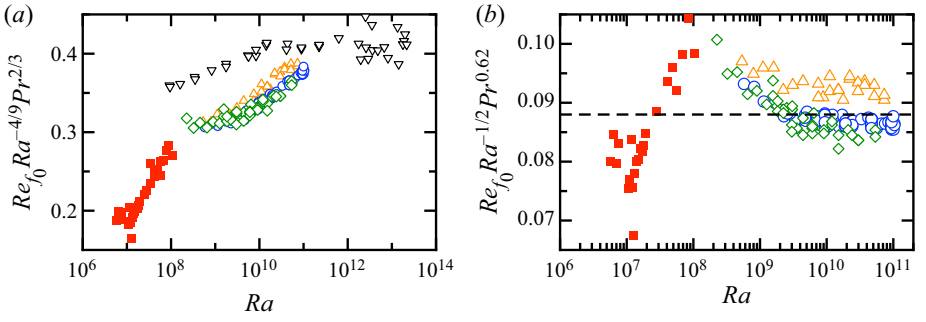

Figure 15. (*a*) Values of Re multiplied by $Ra^{-4/9}Pr^{2/3}$. Squares, this work, cell B, $Pr = 0.72$.; black triangles, from Bruno, run 'C' of Musilová *et al.* (2017), $Pr \sim 1$; orange triangles, from Brown *et al.* (2007), $Pr = 3.32$; circles, from Brown *et al.* (2007), $Pr = 4.38$; diamonds, from Brown *et al.* (2007), $Pr = 5.55$. (*b*) $Re_{f_0} Ra^{-1/2} Pr^{0.62}$ against Ra.

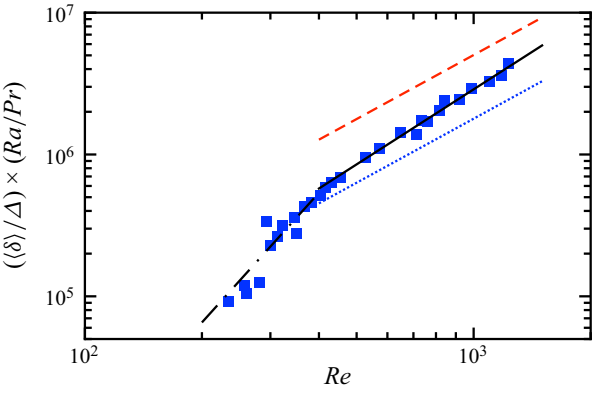

Figure 16. The measured value of $\langle\delta\rangle/\Delta \times Ra/Pr$ as a function of Re. Here, Re_{f_0} is based on the peak frequency of the temperature spectra. Measurements are taken at $\xi = 0.063$, $z/L = 0.51$ in convection cell B. The dotted-dashed line is a power-law fit $\langle\delta\rangle/\Delta \times Ra/Pr = 0.007Re^{3.0\pm0.6}$ to the data $Re < 4.5 \times 10^3$. The solid line is the fit of $\langle\delta\rangle/\Delta \times Ra/Pr = 15.4Re^{1.76\pm0.06}$ to the data $Re > 4.5 \times 10^3$. The dashed line is the fit of $18\pi Re^{3/2}$, the theoretical prediction from Brown & Ahlers (2008*b*). The dotted line is the fit of $159Re^{3/2}$ to the experimental data from figure 9 of Brown & Ahlers (2008*b*) for $Pr = 3.3$, 4.4 and 5.5.

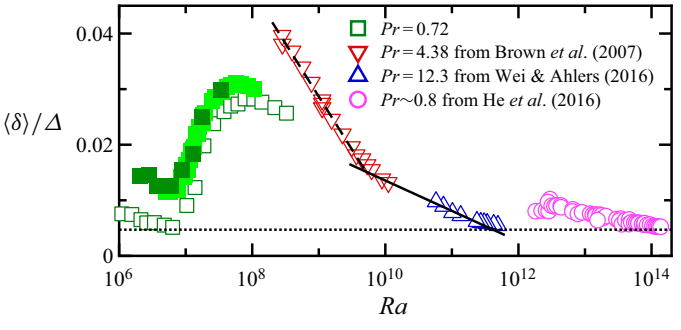

Figure 17. The experimental data of the LSC flow strength against Ra. Open squares, this work from cell A; solid squares, this work from cell B; inverted triangles, data from Brown & Ahlers (2007); triangles, data from Wei & Ahlers (2016); circles, data from He *et al.* (2016). The dotted line is $\langle\delta\rangle/\Delta = 0.0047$, which is the value in conduction regime. The dashed line is $\langle\delta\rangle/\Delta = 0.20 - 0.0083 \log Ra$; The solid line is $\langle\delta\rangle/\Delta = 0.068 - 0.0024 \log Ra$.

$Ra < 2 \times 10^{13}$ and the ultimate regime $Ra > 2 \times 10^{13}$. It is noted that at such large Ra, those authors found $E_1/E_{tot} \sim 0.5$, which is similar to the transition regime. Therefore, it will be interesting to see whether a stronger single-roll structure forms in the RBC with $\Gamma = 1$ and Ra larger than that in He *et al.* (2016).

Another interesting result of the present work is the different responses of the LSC flow strength to the turbulent background in the soft turbulence and hard turbulence regimes. In this context it would be helpful to be able to quantify the turbulent background in some way. However, the temperature measurement in the sidewall does not show any reasonable sign indicating a stronger turbulent background at larger Ra. According to the previous literature, a turbulent background in RBC results in a Gaussian-like temperature distribution at the cell centre whose tails show an exponential trend caused by the thermal plume. Numerous studies have shown that in the soft and hard turbulence regimes, the temperature distribution in the cell centre evolves from a Gaussian function to a stretched exponential function, which reveals that the turbulent background is stronger at larger Ra. Numerous quantities have been proposed to quantify the strength of turbulent backgrounds. Recently, the analytical expression proposed by Wang *et al.* (2019) provided a straightforward quantity, the ratio of the thermal plume strength to the turbulent background strength. However, the plume strength in the cell centre is beyond the scope of the present work, the main measurements of which were taken from the sidewall, and thus, we will not discuss this phenomenon any further here.

5. Summary

In summary, we performed experiments for two $\Gamma = 1$ cylindrical RBC cells with nitrogen gas as the working fluid and measured the flow strength in the horizontal mid-height plane. The Ra range on which we focused extended from $Ra = 1 \times 10^3$ to $Ra = 1 \times 10^9$. From the flow strength, seven regimes were identified: conduction, convection, oscillation, chaotic, transition, soft turbulence and hard turbulence. In the convection regime, the flow forms a pattern corresponding to a single roll. In the oscillation regime, an oscillation frequency showing a peak in the temperature power spectra in the sidewall can be identified. In the chaotic regime, the flow is time-dependent, and the time-averaged flow strength decreases as Ra increases. In the transition regime, the time-averaged flow strength also decreases with increasing Ra. Under soft turbulence, the LSC self-organises, and the flow strength increases with increasing Ra, whereas under hard turbulence, the LSC flow strength decreases as Ra increases. The time-averaged flow strengths in the soft turbulence and hard turbulence regimes are similar to those in the convection and chaotic regimes, suggesting that LSC is an analogy to the cellular pattern at large Ra. This finding also indicates that at the larger Ra of hard turbulence, the LSC will persist and show another sudden change with increasing Ra, similar to the transition regime. However, the difference remains between cellular pattern and LSC, that their preferred orientations are different. In addition, a comparison with other experimental data at larger Ra was made, and the Re based on the LSC turnover time was measured. We found that two power laws, $\langle\delta\rangle/\Delta \times Ra/Pr = 0.007Re^{3.0}$ and $\langle\delta\rangle/\Delta \times Ra/Pr = 15.4Re^{1.76}$, fit our data for $Re < 400$ and for $Re > 400$, respectively. The result lies between the predicted values and the measured values for $Pr > 3$ in water.

Although the present experiment has provided a fairly detailed overall picture of the pattern close to onset of convection and the LSC at high Ra in this system, there remain

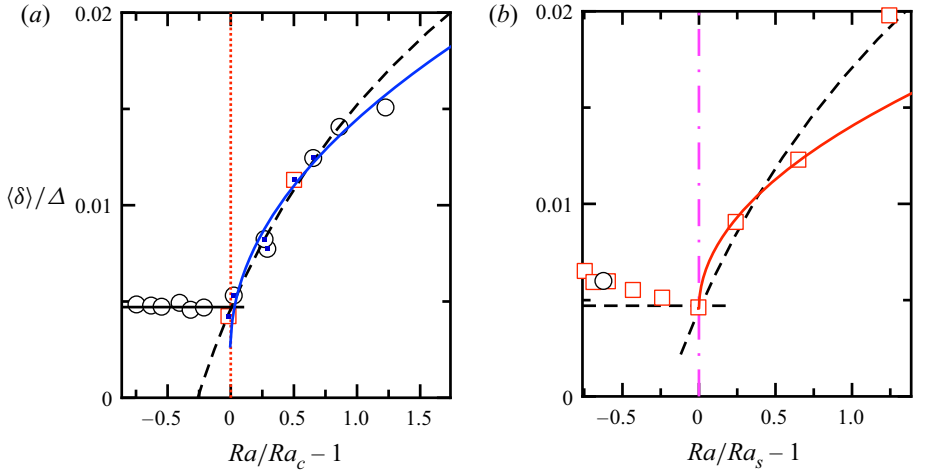

Figure 18. (*a*) The experimental data of the strength of the cellular pattern against $Ra/Ra_c - 1$. Here, $Ra_c = 7300$ was fitted from a logarithmic function for the data $Ra_c \leqslant Ra \leqslant 2Ra_c$, shown as dashed lines. The vertical line represents Ra_c. (*b*) The experimental data of the LSC flow strength against $Ra/Ra_s - 1$. Here, the onset of soft turbulence $Ra_s = 8.38 \times 10^6$ was fitted from a logarithmic function for the data $Ra_s \leqslant Ra \leqslant 2.5Ra_s$, shown by the dashed line. In (*a*,*b*), the dotted line is the value of 0.0047 measured in the conduction regime, which is also considered as the measurement error. The solid lines are fitted by equation $\langle\delta\rangle/\Delta = k(Ra/\eta - 1)^{1/2}$, here $k = 0.012$, $\eta = Ra_C$ for (*a*) and $k = 0.010$, $\eta = Ra_S$ for (*b*).

some unresolved issues. One of them is the dependence of transitions between various regimes on the wall admittance. A more detailed experimental investigation with the other wall admittance should be carried out. Another feature that might be studied in more detail is the Reynolds number based on LSC oscillation frequency in other Pr and larger Ra. The present results of Re are inconsistent with either predicted values or previous measurement in water, and both the Pr and Ra are smaller than in previous work. Of course, as the range of Pr and Ra expands, the richness of phenomena seems without limit.

Acknowledgements. The experiment was conducted in Guenter Ahler's lab at the University of California, Santa Barbara. P.W. is very grateful to G. Ahlers for his guidance.

Funding. The author wishes to acknowledge financial support from the National Natural Science Foundation of China (grant no. 11702196).

Declaration of interests. The author reports no conflict of interest.

Author ORCIDs.
Ping Wei https://orcid.org/0000-0002-2268-9086.

Appendix A. Critical Rayleigh numbers Ra_c and Ra_s

Numerous studies have reported a linear increase in the cellular pattern strength as Ra increases at the onset of convection. However, owing to the limit on the number of data points in our work, a logarithmic function was used to determine Ra_c. To show that fitting the data by a logarithmic function, and fitting them by a function as $k(Ra - Ra_c)^{1/2}$ yield the same result, as in figure 18(*a*), we plot the fits by a logarithmic function and a linear function. The results are in agreement. The same analysis was performed to determine Ra_s, the onset of soft turbulence, as shown in figure 18(*b*). The Ra_s values obtained by the two functions give almost the same result.

Ra	$\langle\delta\rangle/\Delta$	Ra	$\langle\delta\rangle/\Delta$
1.851×10^3	0.00485	2.083×10^4	0.0166
2.690×10^3	0.00478	2.775×10^4	0.0184
3.303×10^3	0.00473	3.570×10^4	0.0195
4.339×10^3	0.00493	4.831×10^4	0.0204
4.984×10^3	0.00457	6.783×10^4	0.0214
5.750×10^3	0.00469	8.426×10^4	0.0202
7.476×10^3	0.00531	1.227×10^5	0.0177
9.258×10^3	0.00824	3.150×10^6	0.0060
9.414×10^3	0.00773	1.653×10^5	0.0192
1.206×10^4	0.0125	2.099×10^5	0.0161
1.358×10^4	0.0141	3.436×10^5	0.0137
1.624×10^4	0.0151	4.890×10^5	0.0104

Table 2. Time-averaged strength $\langle\delta\rangle/\Delta$ as a function of Ra. Cell A, $\Delta = 4.00$ K and $Pr = 0.72$ (circles, figure 10*a*).

Ra	$\langle\delta\rangle/\Delta$	Ra	$\langle\delta\rangle/\Delta$
7.169×10^3	0.00424	6.361×10^6	0.00513
1.096×10^4	0.0113	8.346×10^6	0.00462
2.470×10^4	0.0170	1.039×10^7	0.00906
8.541×10^4	0.0190	1.382×10^7	0.0123
1.460×10^5	0.0203	1.880×10^7	0.0198
2.423×10^5	0.0153	2.630×10^7	0.0238
4.658×10^5	0.00924	3.763×10^7	0.0259
6.670×10^5	0.00754	4.740×10^7	0.0269
1.097×10^6	0.00756	6.098×10^7	0.0273
1.547×10^6	0.00744	7.812×10^7	0.0282
2.126×10^6	0.00652	1.055×10^8	0.0282
2.602×10^6	0.00594	1.395×10^8	0.0277
3.391×10^6	0.00598	2.183×10^8	0.0267
4.763×10^6	0.00553	3.266×10^8	0.0257

Table 3. Time-averaged strength $\langle\delta\rangle/\Delta$ as a function of Ra. Cell A, $\Delta = 10.00$ K and $Pr = 0.72$ (circles, figure 10*a*).

Appendix B. Numerical values of the data shown in figure 10(*a*)

Tables 2 and 3 list the time-averaged strength $\langle\delta\rangle/\Delta$ as a function of Ra plotted in figure 10(*a*).

References

Ahlers, G. 2009 Turbulent convection. *Physics* **2**, 74.

Ahlers, G., Grossmann, S. & Lohse, D. 2009 Heat transfer and large scale dynamics in turbulent Rayleigh–Bénard convection. *Rev. Mod. Phys.* **81**, 503–538.

Bai, K., Ji, D. & Brown, E. 2016 Ability of a low-dimensional model to predict geometry-dependent dynamics of large-scale coherent structures in turbulence. *Phys. Rev.* E **93**, 023117.

Brent, A.D., Voller, V.R. & Reid, K.J. 1988 Enthalpy-porosity technique for modeling convection-diffusion phase change – application to the melting of a pure metal. *Numer. Heat Transfer* **13**, 297–318.

BROWN, E. & AHLERS, G. 2006 Effect of the Earth's Coriolis force on turbulent Rayleigh–Bénard convection in the laboratory. *Phys. Fluids* **18**, 125108.

BROWN, E. & AHLERS, G. 2007 Temperature gradients and search for non-Boussinesq effects in the interior of turbulent Rayleigh–Bénard convection. *Europhys. Lett.* **80**, 14001.

BROWN, E. & AHLERS, G. 2008*a* Azimuthal asymmetries of the large-scale circulation in turbulent Rayleigh–Bénard convection. *Phys. Fluids* **20**, 105105.

BROWN, E. & AHLERS, G. 2008*b* A model of diffusion in a potential well for the dynamics of the large-scale circulation in turbulent Rayleigh–Bénard convection. *Phys. Fluids* **20**, 075101.

BROWN, E., FUNFSCHILLING, D. & AHLERS, G. 2007 Anomalous Reynolds-number scaling in turbulent Rayleigh–Bénard convection. *J. Stat. Mech.* **2007**, P10005.

BROWN, E., NIKOLAENKO, A. & AHLERS, G. 2005*a* Reorientation of the large-scale circulation in turbulent Rayleigh–Bénard convection. *Phys. Rev. Lett.* **95**, 084503.

BROWN, E., NIKOLAENKO, A., FUNFSCHILLING, D. & AHLERS, G. 2005*b* Heat transport by turbulent Rayleigh–Bénard convection: effect of finite top- and bottom-plate conductivity. *Phys. Fluids* **17**, 075108.

BUELL, J.C. & CATTON, I. 1983 Effects of rotation on the stability of a bounded cylindrical layer of fluid heated from below. *Phys. Fluids* **26**, 892.

BUSSE, F.H. 2003 The sequence-of-bifurcations approach towards understanding turbulent fluid flow. *Surv. Geophys.* **24**, 269–288.

CHANDRA, M. & VERMA, M.K. 2011 Dynamics and symmetries of flow reversals in turbulent convection. *Phys. Rev.* E **83**, 067303.

CHANDRA, M. & VERMA, M.K. 2013 Flow reversals in turbulent convection via vortex reconnections. *Phys. Rev. Lett.* **110**, 114503.

CHARLSON, G.S. & SANI, R.L. 1970 Thermoconvective instability in a bounded cylindrical fluid layer. *Intl J. Heat Mass Transfer* **13**, 1479–1496.

CHARLSON, G.S. & SANI, R.L. 1971 On thermoconvective instability in a bounded cylindrical fluid layer. *Intl J. Heat Mass Transfer* **14**, 2157–2160.

FOROOZANI, N., NIEMELA, J.J., ARMENIO, V. & SREENIVASAN, K.R. 2017 Reorientations of the large-scale flow in turbulent convection in a cube. *Phys. Rev.* E **95**, 033107.

FUNFSCHILLING, D., BROWN, E. & AHLERS, G. 2008 Torsional oscillations of the large-scale circulation in turbulent Rayleigh–Bénard convection. *J. Fluid Mech.* **607**, 119–139.

HARTLEP, T., TILGNER, A. & BUSSE, F.H. 2005 Transition to turbulent convection in a fluid layer heated from below at moderate aspect ratio. *J. Fluid Mech.* **544**, 309–322.

HARTMANN, D.L., MOY, L.A. & FU, Q. 2001 Tropical convection and the energy balance at the top of the atmosphere. *J. Clim.* **14**, 4495–4511.

HE, X., BODENSCHATZ, E. & AHLERS, G. 2016 Azimuthal diffusion of the large-scale-circulation plane, and absence of significant non-Boussinesq effects, in turbulent convection near the ultimate-state transition. *J. Fluid Mech.* **791**, R3.

HÉBERT, F., HUFSCHMID, R., SCHEEL, J. & AHLERS, G. 2010 Onset of Rayleigh–Bénard convection in cylindrical containers. *Phys. Rev.* E **81** (4), 046318.

HESLOT, F., CASTAING, B. & LIBCHABER, A. 1987 Transition to turbulence in helium gas. *Phys. Rev.* A **36**, 5870–5873.

HUNT, G.R. & LINDEN, P.F. 1999 The fluid mechanics of natural ventilation – displacement ventilation by buoyancy-driven flows assisted by wind. *Build. Environ.* **34**, 707–720.

JEFFREYS, H. 1928 Some cases of instability in fluid motion. *Proc. R. Soc. Lond.* A **118** (779), 195–208.

JI, D. & BROWN, E. 2020 Low-dimensional model of the large-scale circulation of turbulent Rayleigh–Bénard convection in a cubic container. *Phys. Rev. Fluids* **5**, 064606.

KRISHNAMURTI, R. & HOWARD, L.N. 1981 Large scale flow generation in turbulent convection. *Proc. Natl Acad. Sci. USA* **78**, 1981–1985.

LOHSE, D. & XIA, K.-Q. 2010 Small-scale properties of turbulent Rayleigh–Bénard convection. *Annu. Rev. Fluid Mech.* **42**, 335–364.

MAMYKIN, A.D., KOLESNICHENKO, I.V., PAVLINOV, A.M. & KHALILOV, R.I. 2018 Large scale circulation in turbulent Rayleigh–Bénard convection of liquid sodium in cylindrical cell. *J. Phys.: Conf. Ser.* **1128**, 012019.

MARSHALL, J. & SCHOTT, F. 1999 Open-ocean convection: observations, theory, and models. *Rev. Geophys.* **37**, 1–64.

MISHRA, P.K., DE, A.K., VERMA, M.K. & ESWARAN, V. 2011 Dynamics of reorientations and reversals of large-scale flow in Rayleigh–Bénard convection. *J. Fluid Mech.* **668**, 480–499.

MUELLER, K.H., AHLERS, G. & POBELL, F. 1976 Thermal expansion coefficient, scaling, and universality near the superfluid transition of ^{4}He under pressure. *Phys. Rev.* B **14**, 2096–2118.

MÜLLER, G., NEUMANN, G. & WEBER, W. 1984 Natural convection in vertical bridgeman configurations. *J. Cryst. Growth* **70**, 78–93.

MUSILOVÁ, V., KRÉALÍÍK, T., LA MANTIA, M., MACEK, M., URBAN, P. & SKRBEK, L. 2017 Reynolds number scaling in cryogenic turbulent Rayleigh–Bénard convection in a cylindrical aspect ratio one cell. *J. Fluid Mech.* **832**, 721–744.

NI, R., HUANG, S.-D. & XIA, K.-Q. 2015 Reversals of the large-scale circulation in quasi-2D Rayleigh–Bénard convection. *J. Fluid Mech.* **778**, R5.

RAHMSTORF, S. 2000 The thermohaline ocean circulation: a system with dangerous thresholds? *Clim. Change* **46**, 247–256.

SAKIEVICH, P.J., PEET, Y.T. & ADRIAN, R.J. 2016 Large-scale thermal motions of turbulent Rayleigh–Bénard convection in a wide aspect-ratio cylindrical domain. *Intl J. Heat Fluid Flow* **61**, 183–196, sI TSFP9 special issue.

SCHLÜTER, A., LORTZ, D. & BUSSE, F.H. 1965 On the stability of steady finite amplitude convection. *J. Fluid Mech.* **23** (1), 129–124.

SREENIVASAN, K.R., BERSHADSKI, A. & NIEMELA, J.J. 2002 Mean wind and its reversals in thermal convection. *Phys. Rev.* E **65**, 056306.

STORK, K. & MÜLLER, U. 1975 Convection in boxes: an experimental investigation in vertical cylinders and annuli. *J. Fluid Mech.* **71**, 231–240.

SUGIYAMA, K., NI, R., STEVENS, R.J.A.M., CHAN, T.S., ZHOU, S.-Q., XI, H.-D., SUN, C., GROSSMANN, S., XIA, K.-Q. & LOHSE, D. 2010 Flow reversals in thermally driven turbulence. *Phys. Rev. Lett.* **105**, 034503.

THRELFALL, D.C. 1975 Free convection in low temperature gaseous helium. *J. Fluid Mech.* **67**, 17–28.

VOGT, T., HORN, S., GRANNAN, A.M. & AURNOU, J.M. 2018 Jump rope vortex in liquid metal convection. *Proc. Natl Acad. Sci. USA* **115** (50), 12674–12679.

WAGNER, S. & SHISHKINA, O. 2013 Aspect-ratio dependency of Rayleigh–Bénard convection in box-shaped containers. *Phys. Fluids* **25** (8), 085110.

WAN, Z.-H., WEI, P., VERZICCO, R., LOHSE, D., AHLERS, G. & STEVENS, R.J.A.M. 2019 Effect of sidewall on heat transfer and flow structure in Rayleigh–Bénard convection. *J. Fluid Mech.* **881**, 218–243.

WANG, Y., HE, X.-Z. & TONG, P. 2019 Turbulent temperature fluctuations in a closed Rayleigh–Bénard convection cell. *J. Fluid Mech.* **874**, 263–284.

WEI, P. & AHLERS, G. 2016 On the nature of fluctuations in turbulent Rayleigh–Bénard convection at large Prandtl numbers. *J. Fluid Mech.* **802**, 203–244.

WEISS, S. & AHLERS, G. 2011 Turbulent Rayleigh–Bénard convection in a cylindrical container with aspect ratio $\gamma = 0.50$ and Prandtl number $Pr = 4.38$. *J. Fluid Mech.* **676**, 1–4.

WEISS, S., WEI, P. & AHLERS, G. 2016 Heat-transport enhancement in rotating turbulent Rayleigh–Bénard convection. *Phys. Rev.* E **93**, 043102.

XI, H.-D. & XIA, K.-Q. 2007 Cessations and reversals of the large-scale circulation in turbulent thermal convection. *Phys. Rev.* E **75**, 066307.

XI, H.-D. & XIA, K.-Q. 2008 Flow mode transition in turbulent thermal convection. *Phys. Fluids* **20**, 055104.

XI, H.-D., ZHANG, Y.-B., HAO, J.-T. & XIA, K.-Q. 2016 Higher-order flow modes in turbulent Rayleigh–Bénard convection. *J. Fluid Mech.* **805**, 31–51.

XI, H.D., ZHOU, Q. & XIA, K.Q. 2006 Azimuthal motion of the mean wind in turbulent thermal convection. *Phys. Rev.* E **73**, 056312.

XI, H.-D., ZHOU, S.-Q., ZHOU, Q., CHAN, T.-S. & XIA, K.-Q. 2009 Origin of the temperature oscillation in turbulent thermal convection. *Phys. Rev. Lett.* **102**, 044503.

XIE, Y.-C., WEI, P. & XIA, K.-Q. 2013 Dynamics of the large-scale circulation in high-Prandtl-number turbulent thermal convection. *J. Fluid Mech.* **717**, 322–346.

YANAGISAWA, T., YAMAGISHI, Y., HAMANO, Y., TASAKA, Y. & TAKEDA, Y. 2011 Spontaneous flow reversals in Rayleigh–Bénard convection of a liquid metal. *Phys. Rev.* E **83**, 036307.

ZHOU, Q., XI, H.-D., ZHOU, S.-Q., SUN, C. & XIA, K.-Q. 2009 Oscillations of the large-scale circulation in turbulent Rayleigh–Bénard convection: the sloshing mode and its relationship with the torsional mode. *J. Fluid Mech.* **630** (-1), 367–390.